

Flow Visualization of a Scramjet Inlet - Isolator Model in Supersonic Flow

S. Seckin¹, K.B. Yuceil²

¹Graduate Student, Dept. of Astronautical Engineering, Istanbul Technical University, 34469 Maslak, Istanbul, Turkey

²Asst Prof., Dept. of Astronautical Engineering, Istanbul Technical University, 34469 Maslak, Istanbul, Turkey

Abstract. Understanding the physical mechanisms and having insight to the complex flowfield involving unstart phenomena in supersonic inlets has gained considerable attention especially in the area of scramjet inlet/isolator aerothermodynamics. In this study, Schlieren visualization and computational analysis of shock wave structures in ramjet/scramjet inlet/isolator models in supersonic flow have been performed. Experiments were performed in the supersonic wind tunnel at the Trisonic Research Laboratory in Istanbul Technical University. The test section floor and the existing mechanism underneath have been modified to be able to mount the designed inlet/isolator model on the floor of the test section. The inlet/isolator model with a 12-degree compression ramp is investigated at Mach 2 both computationally and experimentally. Computations were performed using Star-CCM+ software to investigate shock wave structures in and around the three dimensional inlet/isolator model as mounted on the test section floor as a guide for designing the experimental model. In the results, the effects of shock wave – boundary layer interactions with flow separations with were observed. Ensemble average of the density distributions on a series of planes from one side wall to the other from the CFD results agreed well with the Schlieren images obtained experimentally. The structure of the shock waves and angles obtained from the Schlieren images agree quite well with those obtained from the CFD results. The effects of lambda-shock formations which indicate possible boundary layer separations, reflections of shock waves, and shock wave – boundary layer interactions on inlet unstart phenomena have been discussed. In order to investigate inlet unstart mechanism further, different experimental setups have been suggested for future work.

1 Introduction

Developing reliable and affordable ramjet and scramjet propulsion technologies is vital for realizing routine supersonic and hypersonic transport. Ramjet/Scramjet engines are air-breathing engines that use the surrounding air as a working fluid. High Mach number air is first slowed down and compressed by the inlet/isolator prior to mixing with fuel and then sent to the combustor. Hot exhaust gases pass through a nozzle and produce thrust. Ramjet/Scramjet uses forward motion of the vehicle to compress incoming air at the inlet instead of a rotary compressor in conventional jet engines. Therefore, they have less moving parts and they are much lighter than turbine engines.

In ramjet, air is slowed down to subsonic speeds by a system of shock waves in the inlet/isolator. Therefore, the combustion takes place at subsonic speeds. Hot combustion gases are accelerated through a convergent-divergent nozzle to supersonic speeds. Inefficiencies regarding performance losses occur due to shock waves in the inlet/isolator. Also, thermal and mechanical loads

increase on the combustion chamber walls. Because of these performance limitations, ramjet propulsion is not suitable speeds above Mach 5 [1].

In scramjet (supersonic combustion ramjet), although the incoming flow is slowed down and compressed through the inlet, combustion process occurs supersonically. Therefore, the engine is less susceptible to total pressure losses than the ramjet due to weaker shock waves and is relatively more efficient for hypersonic flight. Also compared to rockets, which must carry their own oxidizer, scramjet engines are more efficient for a flight in the atmosphere [2]. Developing scramjet technologies will lead to vehicles with affordable and reusable air-breathing hypersonic engines such as cruise missiles; long range aircraft and space-access vehicles for taking off and landing such as airliners [3].

In figure 1 a schematic of a scramjet is shown. Forebody provides the first compression of airflow. Shock waves in the inlet/isolator convert the dynamic pressure due to the velocity of incoming air into higher

static pressure. The shock train can be seen clearly in figure 1 and Mach number is reduced while static pressure and temperature increase along the isolator through shock waves.

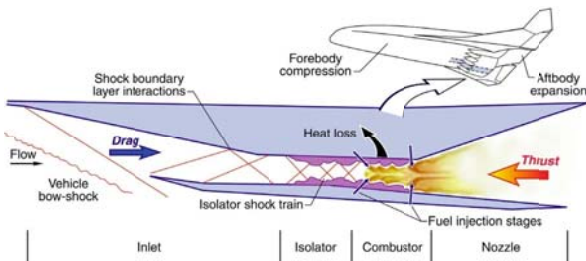


Fig. 1. Schematic of a scramjet [4].

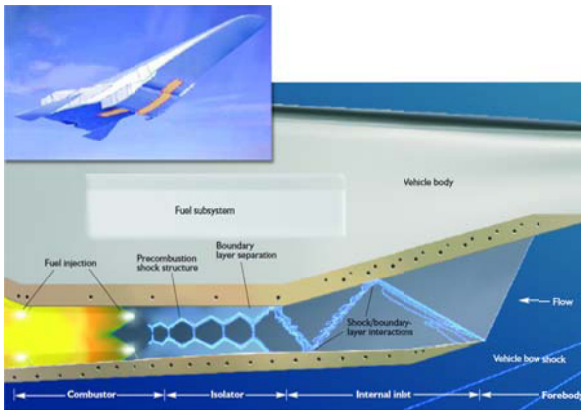


Fig. 2. Scramjet components [3].

For ramjet/scramjet, isolator is a critical component that adjusts the static back-pressure. At the beginning of the combustion, boundary layer starts to separate and a precombustion shock appears in the isolator as shown in in figure 2 [3]. Due to instabilities in the combustion process, static back-pressure changes in the isolator. The pressure rise can force the shock waves to be pushed out of the isolator and inlet. This condition is called inlet unstart which produces undesirable inlet conditions and may lead to more catastrophic consequences such as engine failure.

Hypersonic vehicles are subject to several extraordinary challenges for both structural and material aspects. These are [3]:

- Very high temperatures
- Heating of the whole vehicle
- Steady-state and transient localized heating from shock waves
- High aerodynamic loads
- High fluctuating pressure loads
- The potential for severe flutter, vibration, fluctuating and thermally induced stresses
- Erosion from air flow over the vehicle and through the engine

By developing technology, new research on materials and more experiments are done on scramjet

propulsion, hypersonic flight will be available both for space access and long distance transportation in the future.

Curran and Stull [5] proposed the dual-mode engine concept in which the engine is allowed to act in ramjet mode at lower supersonic flight Mach numbers and then transition to scramjet mode at higher supersonic to hypersonic flight Mach numbers. Since the dual-mode proposal in 1963, much work has been done for understanding the complex flowfields involved, improving the performance of such engines, and developing methods of practical implementation [6–20].

More recently, optical flow diagnostics such as high speed Schlieren and PIV have been used to investigate the unstart process in an inlet-isolator model at Mach 5 and found out that unstart was strongly influenced by the geometry and the separated flow resulting from shock wave boundary layer interactions [21,22].

In order to initiate and build the infrastructure for the studies on scramjet inlet unstart at Istanbul Technical University a preliminary work has been done in the current study. Wind tunnel test section has been modified to allow for mounting supersonic inlet models on the floor and provisions have been made to add further capabilities to initiate unstart in such models. This study summarizes some of the efforts made in that direction including shock wave visualization by schlieren method and the computational analysis which are performed to improve the process of designing and manufacturing the experimental model to be used in the wind tunnel.

2 Experimental Setup

2.1 Mounting apparatus setup and modifications

Experiments were carried out in the 15×15 cm Trisonic Wind Tunnel at Istanbul Technical University. The tunnel is a blow-down type and has two Mach number ranges achieved by using two different nozzle-test section blocks with ranges of 0.4 – 2.1, and 0.4 – 4.0. In the present study, the test section with the range 0.4 – 2.1 is used and the Mach number is set to 2.0 for the visualization experiments. The tunnel has two circular windows made of quartz for schlieren visualization on its side walls and perforated floor and ceiling for boundary layer suction in transonic flow regime. The presence of the perforated floor and ceiling and the boundary layer mechanism prevents mounting the models on either upper or lower walls.

The tunnel has a stick-type support for mounting axisymmetric models in the center of the test section. However, the inlet model used in the experiments is not suitable for mounting to the support due to its non-axisymmetric shape and off-center point of attachment in the back of the model. Because of these inconveniences the inlet/isolator model is mounted on the wind tunnel floor using a set of floor plugs, which was designed to

replace the original tunnel floor with its boundary layer suction mechanism. Figure 3 shows the new solid stainless steel floor plug (labeled as 1) which replaces the original perforated brass floor of the wind tunnel. It is redesigned as having a slot to accommodate a thicker inner plug (labeled as 2 in figure 3) for attaching the model from the bottom and underneath the floor as shown in figure 3. This inner plug also allows mounting different models without having to change the new floor piece and can be replaced with another one with optical access.

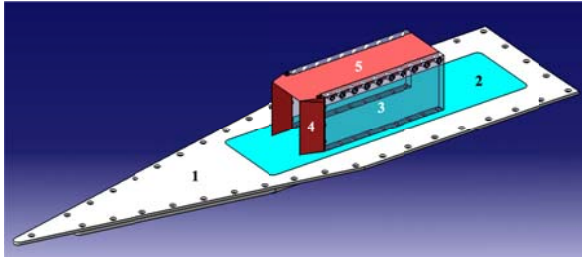


Fig. 3. Mounting apparatus and inlet/isolator model assembly.

In the present study, the model is a simple duct that has an inlet with a ramp providing entrance and compression of incoming air flow, and a straight isolator section representing the link to the combustion chamber of a scramjet engine. The designed inlet/isolator model represents a ramjet/scramjet inlet that is mounted under the body of an aircraft. The lower wall of the wind tunnel acts as the forebody of the vehicle. Figure 4 shows a photo of the model mounted on the wind tunnel.



Fig. 4. Test section module for Mach 2 and the designed inlet/isolator model assembly.

2.2 Inlet/Isolator design and calculations

Inlet design of a ramjet/scramjet is critical due to primary shock wave formation and the resulting compression of the incoming air. The mechanism that creates shock wave is a ramp which deflects incoming air flow. As shown in figure 5, incoming air flow at M_1 goes through an oblique shock wave with angle β due to the

ramp and the flow deflects by an angle of θ with a speed M_2 where M_{n1} and M_{n2} are the Mach number components normal to the shock for M_1 and M_2 , respectively. Relationship between the deflection angle, shock angle and the incoming Mach number is given by

$$\tan \theta = 2 \cot \beta \frac{M_1^2 \sin^2 \beta - 1}{M_1^2 (\gamma + \cos 2\beta) + 2} \quad (1)$$

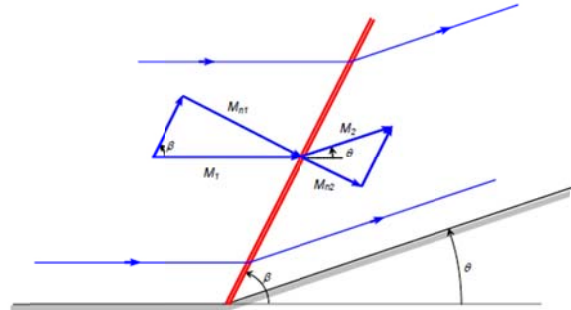


Fig. 5. Oblique Shock Geometry.

Since the experiments are carried out at Mach 2, the maximum determined ramp angle θ from equation (1) is about 22.97° for air. Therefore, all the ramps of the inlet model facing the freestream, should be smaller than this maximum angle because when the maximum θ angle is exceeded, a detached bow shock wave is formed. Detached bow shock wave is an undesired condition for ramjet/scramjet because it can lead to inlet unstart and the flow behind the shock wave becomes subsonic.

In order to keep the velocity behind the first shock in supersonic range, ramp angle of the inlet model is chosen as 12° as shown in figure 6 where the flow direction is from left to the right. In order to be able to observe shock wave reflections, the total length of the inlet/isolator model is 160 mm. To observe at least two reflections, and to prevent shock wave boundary layer interactions and inlet unstart, the height is set to 50 mm with the help of Computational Fluid Dynamics (CFD) analyses which will be discussed in further sections.

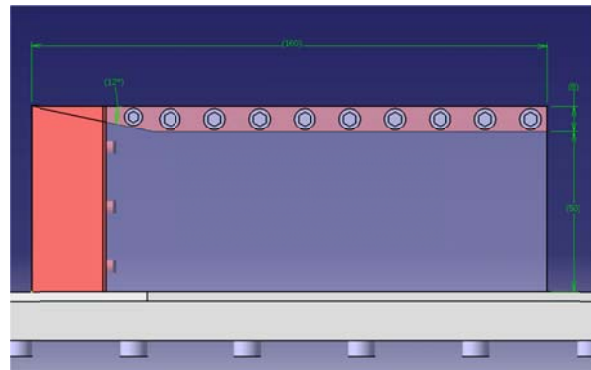


Fig. 6. Schematic side view of the inlet/isolator model.

For the first shock wave, downstream Mach number can be obtained for $M_1 = 2$ and $\theta = 12^\circ$ ramp angle using shock wave theory as 1.565 which is still supersonic.

When viewed from the top, the outer ramp angles of the side walls of the model have been chosen as 20° which is again below θ_{\max} for $M = 2$ as shown in figure 7. To be able to start the wind tunnel, the blockage ratio, which is the total projection area of the model divided by test section area, should be below 15%. The ratio for the designed inlet/isolator model is about 5.7% which satisfies the required condition.

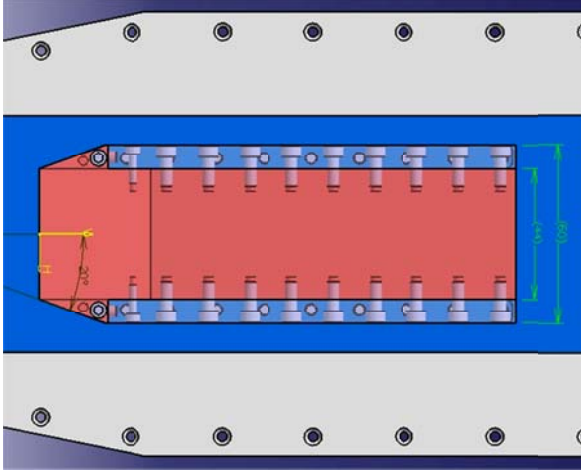


Fig. 7. Top view of the inlet/isolator model.

The inlet/isolator model was designed as consisting of 5 pieces for the sake of manufacturing simplicity. The parts numbered by 4 and 5 in figure 3 were made of brass due to strength considerations and the number 3 was made of Plexiglas since it had to be transparent to visualize shock waves with the Schlieren method.

Also to minimize the interference in the flow, all the fasteners were embedded. Due to the pressure differences on the walls between the inside and the outside of the inlet/isolator liquid sealant was used between the connections of the parts to prevent any leakage. In order to provide a smooth airflow around the model the small cavities in the heads of bolts were filled with model wax as shown in figure 8.

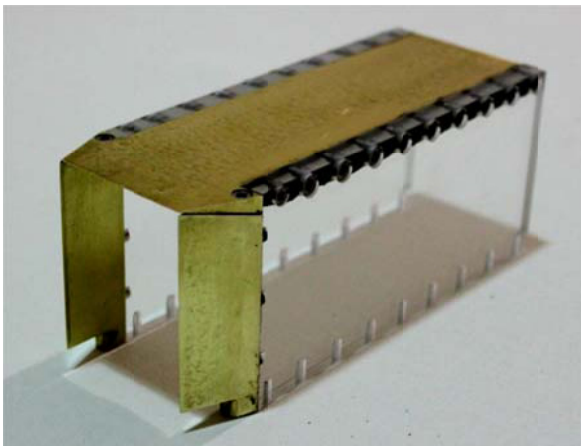


Fig. 8. Inlet/isolator model assembly.

3 Computational Configurations

For the analysis of the flow in and around the inlet/isolator model and the wind tunnel test section, Star-CCM+ software was used. First, a 2D coarse solution of the problem was carried out to understand the characteristics of shock waves and expansion waves. Afterwards, a 3D fine solution was employed. Details of these studies will be explained in further sections.

3.1 2D CFD Analysis

The problem was run with 43293 cells and 86198 faces. For Mach 2, the physical model was selected as:

- Two Dimensional
- Inviscid
- Gas
- Coupled Flow
- Ideal Gas
- Coupled Energy
- Steady

This fast solution with a coarse mesh was done to decide the dimensions of the experimental model. As shown in figure 9 at least two reflections were observed. Since y -momentum of the residuals was not converged enough, solution at the back side area of the isolator is somewhat artificial and does not represent the correct situation.

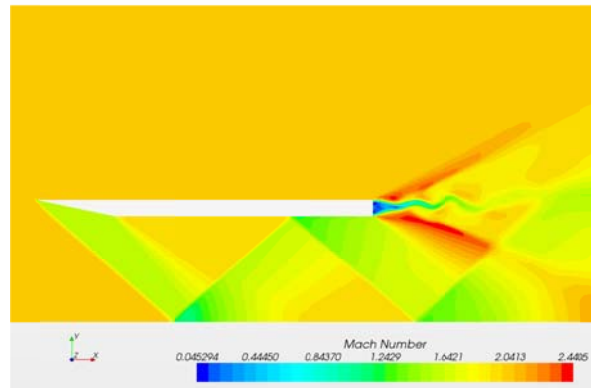


Fig. 9. Mach number distribution of the 2D inlet/isolator model.

3.2 3D CFD Analysis

Since the actual flow is 3D, viscous and turbulent, a much better defined case was run. First, the volume that fluid flows is modeled as solid and the CAD model was imported into Star-CCM+ as shown in figure 10.

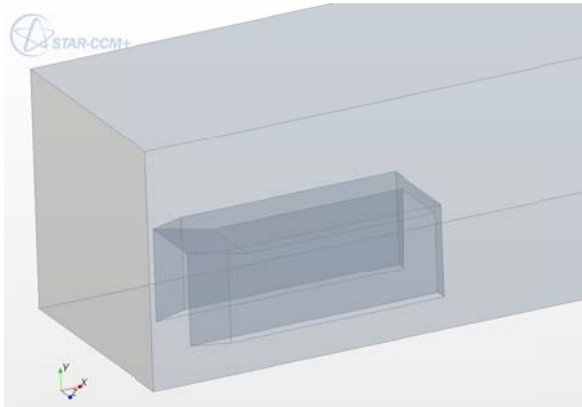


Fig. 10. CAD model of the flow region.

For the computational grid hexahedral mesh type was selected since it was suitable for this kind of flows. Since the flow is viscous, to observe the shock - boundary layer interactions and flow separations, Prism Layer Mesher was selected in the Meshing Models option. Also Trimmer and Surface Remesher were selected for a good volume mesh.

Fine mesh is not required in everywhere within the computational domain; therefore in order to decrease the number of cells and save computation time, five regions were created with mesh sizes becoming bigger in every step. Maximum Cell Sizes of the regions were set to 1, 4, 16, 32 and 64 mm in that order. Prism Layer Thicknesses on the walls were set to 2 mm and Prism Layer Stretching was set as 1.1. Number of Prism Layers was defined as 20, which created twenty layers in the defined boundary layer thickness. Also for a slow transition of surface cell size between different regions, Surface Grow Rate was set to 1.1 and Template Grow Rate was set as slow.

The resulting mesh consists of 7307598 cells and 21864559 faces as shown in figure 11 from three different views. The back side of the model was kept long in order to have better convergence for better results and this also prevented the reverse flow warnings during iteration.

For the Physical Models selection, the following were chosen to define the physical conditions in the code:

- Three Dimensional
- Gas
- Coupled Flow
- Ideal Gas
- Coupled Energy
- Turbulent
- Reynolds-Averaged Navier-Stokes
- Spalart-Allmaras Turbulence
- Standard Spalart-Allmaras
- All y^+ Wall Treatment
- Steady

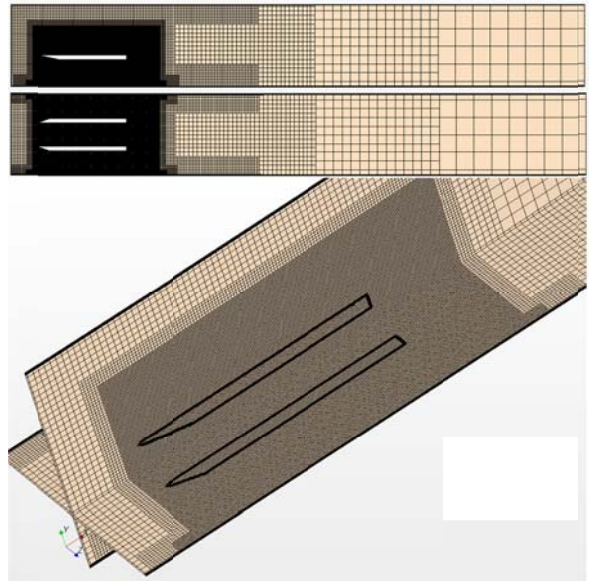


Fig. 11. Grid structure from different views.

This problem is analyzed using the following assumptions. First of all it was assumed that the flow was steady and the fluid was standard air as ideal gas. Also the flow is turbulent and Spalart-Allmaras turbulence model was used. For the turbulent boundary layer y^+ Wall Treatment was selected.

In the CFD model the entrance of the flow to the tunnel is defined as inlet and the exit from the tunnel is defined as outlet. In order to define the boundary conditions for inlet and outlet, isentropic flow equations are used for a freestream Mach number of 2. Flow conditions which are selected to match the experimental conditions are obtained as 160 K for the static temperature of the airflow at the inlet and 33670 Pa as Reference Pressure. Also outlet static temperature was defined as 288 K. For a fast solution of the problem, an initial 500 m/s velocity in the x -direction, which is very close to the two times the speed of sound is defined as initial condition.

Even if it takes more time to solve, for a better convergence, Courant Number, which is also known as CFL number, is taken as 0.1 for this problem. After 1270 steps, it was observed that shock waves settled enough.

3.3 3D CFD Analysis Results

When viewed from the side as shown in figure 12 Mach number distribution clearly shows the shock waves. Across the first shock wave Mach number decreases but with the help of the expansion wave, flow speeds up again where it reaches nearly to the free stream Mach number. But, in the regions where shock wave interacts with boundary layer, the flow slows down. Because of the pressure difference between upstream and the downstream of the shock wave, boundary layer thickness increases significantly especially in the area of interaction

with the first shock wave since it is the strongest of all shock waves. This thick boundary layer acts as a bump on the wall and for this reason another shock wave appears. Shock waves continue by reflecting along x -direction and their strength decrease. Also as shown in figure 13 boundary layer separation can be observed clearly for the first shock wave – boundary layer interaction. The velocity vectors that point in the negative x -direction is the indication for the boundary layer separation. The red region in figure 12 can be misleading because due to the expansion waves at the back and the reflection from the side walls of the wind tunnel, Mach number appears as maximum in this area which does not represent the real situation in the flow rather than the wind tunnel.

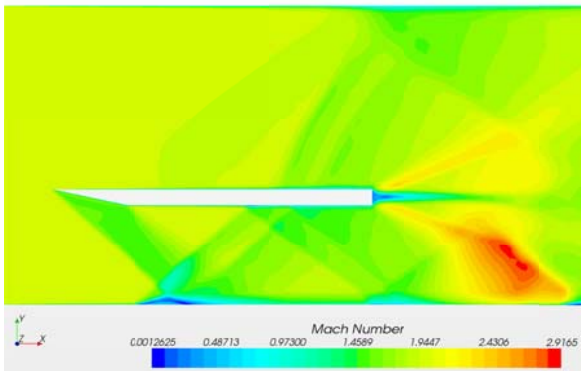


Fig. 12. Shock waves and Mach number distribution from side view.

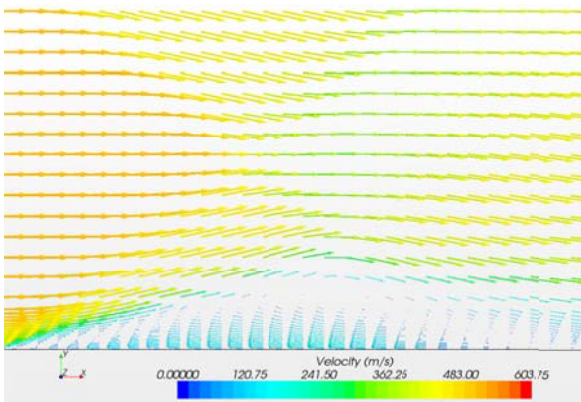


Fig. 13. Boundary layer separation vectors.

When viewed from the top, similar conditions are observed as shown in figure 14. Since the deflection angle at the tip from the top view is higher than the angle of the ramp from the side view, the shock wave appears to be stronger as shown clearly in figure 14.

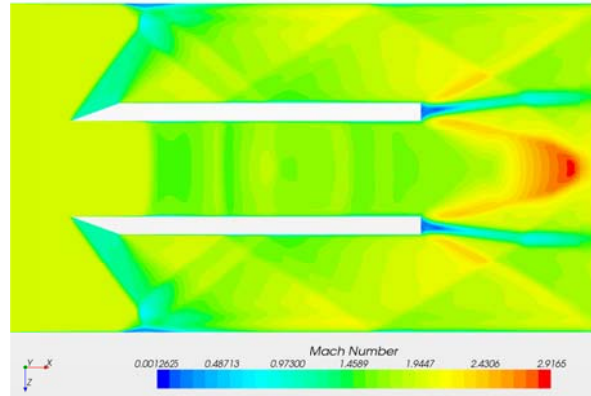


Fig. 14. Mach number distribution from the top view.

Using density distribution to visualize the results of the CFD analysis has been considered appropriate since the Schlieren method is related with the density gradients. As shown in figure 15, the density distributions from the side view help understand the shock wave structures better due to the sudden density change across the shock wave. By starting from the centerline, side view cross sections of the density distribution are shown in figure 9 numbered from 1 to 8. Number 1 represents center and number 2 represents the cross section 10 mm away from the center in the spanwise z -direction. The 10 mm spacing continues until number 8 which represents 70 mm away from the center and the wall of the wind tunnel is at 75 mm. Since the solution is symmetric with respect to the center plane, only one side is enough to analyze the problem. From number 1 to number 3, shock waves and reflections can be clearly observed in the inlet/isolator. Number 4 is the cross section where outer side of the inlet/isolator vertical wall. This shows the shock wave profile of the 20° angle tip ramp of the side walls in the front. Numbers from 5 to 8 show the shock wave structure between outside of the inlet/isolator and the wind tunnel side wall. Since the light rays in the Schlieren method go through the z -direction, the resultant image is affected by all cross sectional regions. Therefore, the average of all the solution of the cells from one side to the other side of the wind tunnel side walls were calculated by exporting results to Tecplot and creating the average final image by using Matlab. The expected Schlieren image is shown in figure 16 and it is compared with experimental results in the further sections.

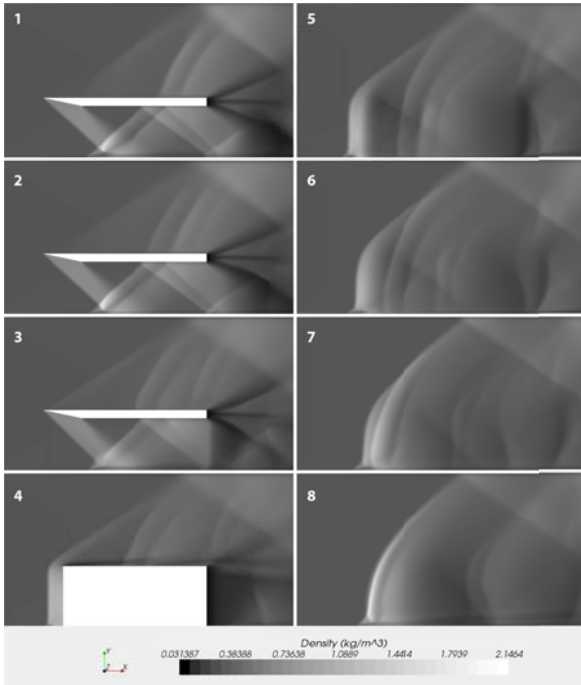


Fig. 15. Density distributions from the side view.

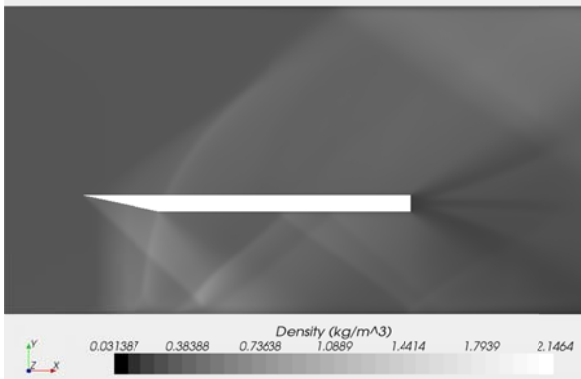


Fig. 36. Average density distribution along z-direction.

4 Experimental Results

Experiments were performed at Mach 2 in the supersonic wind tunnel in the Trisonic Research Laboratory at the Faculty of Aeronautics and Astronautics of Istanbul Technical University. In the repeated experiments nearly the same results were obtained as shown in figure 17.

As calculated in the previous sections for Mach 2 and 12° ramp angle, from equation (1), β angle is 41.6°. Also for Mach 2 the angle of the Mach wave is calculated as:

$$\mu = \sin^{-1} \frac{1}{M} = \sin^{-1} \frac{1}{2} = 30^\circ$$

The structure of the shock waves is drawn schematically in figure 18 and the angles do not represent exact values. According to the approximate sketch, the line originating from the tip of the 12° ramp as numbered

by 1 is a shock wave because the angle is close to the calculated β angle compared to the Mach angle, μ , and this shock wave interacts with boundary layer on the tunnel floor. Because of this interaction, a lambda-shock forms in this region. It is clearly shown that shock structure of the CFD results in figure 19 is very similar to the experimental results in figure 18. A similar but smaller lambda-shock is formed in the CFD results since the boundary layer in CFD analysis is much thinner compared to that of the wind tunnel walls. Lambda shocks are the indicators of the possibility of boundary layer separations. As mentioned in the previous sections, boundary layer separations were observed in figure 13 with the reverse velocity vector profiles. Therefore, in the experiments an extensive boundary layer separation occurs as indicated by such a big lambda shock formation.



Fig. 47. Schlieren image of the inlet/isolator at Mach 2.

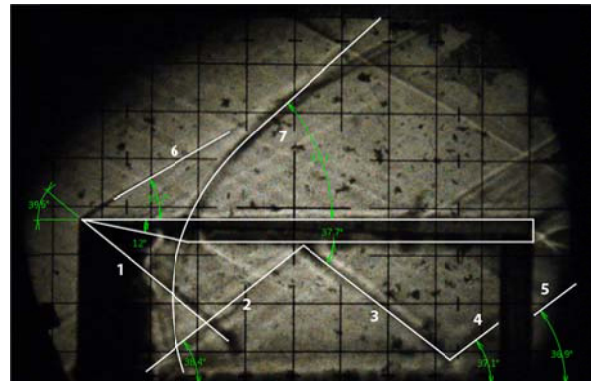


Fig. 18. Shock wave structure from the experimental result.

The shock wave numbered by 1 reflects and the shock wave number 2 is formed. This reflection continues on until the shock number 4 is formed. In fact, the shock waves numbered by 4 and 5 are the same but it looks as if they are different from each other because this is caused by the refraction of the light by Plexiglas side walls of the inlet/isolator. The angle of the wave number 6 is very close to that of a Mach wave and it is probably a Mach wave or a weak shock. Number 7 is formed due to the outer tip with an angle of 20° of the side walls of the inlet/isolator and it is between inlet/isolator walls and wind tunnel inner walls. This shock wave can be observed better in figure 15 from images through 5 to 8.

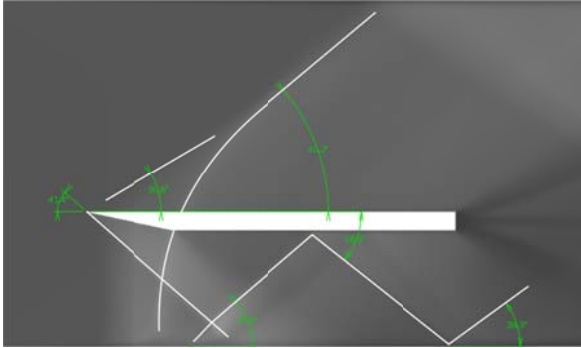


Fig. 19. Shock wave structure in the CFD results.

In summary, when shock waves interact with boundary layers, the thickness of the boundary layer increases and lambda-shocks occur as a result of flow separations. A second shock wave forms at the back of the separated boundary layer. In order to understand and prevent unstart, shock-induced boundary layer separations should be investigated in more detail.

5 Conclusion

In this paper, a supersonic inlet/isolator model is investigated at Mach 2 both computationally and experimentally. With the help of CFD analysis the shock wave structure of the inlet/isolator is obtained. The interaction between shock waves and boundary layers shows the possibility of flow separations. Also shock waves have a big effect on increasing the boundary layer thickness. This thickened boundary layer can cause the formation of a second shock wave. All of these effects have an important role on inlet unstart which may occur at supersonic Mach numbers. For the future work, by placing a flap in back of the isolator and adjusting the flap angle, unstart conditions can be induced and investigated further. Particle Image Velocimetry (PIV) technique can be used to obtain quantitative information about the flow field within the inlet/isolator. Also unsteady surface pressure measurements within the inlet can be performed to gain a better idea about the dynamic behavior of the flow and the unstart process.

References

1. *Ramjet Propulsion*. (n.d.). Retrieved April 2012, from NASA: <http://www.grc.nasa.gov/WWW/k-12/airplane/ramjet.html>
2. *Scramjet Propulsion*. (n.d.). Retrieved April 2012, from NASA: <http://www.grc.nasa.gov/WWW/k-12/airplane/scramjet.html>
3. D. Andreadis, *The Industrial Physicist*, **AugSep**, 24-27, (2004)
4. *How Scramjets Work*. (n.d.). Retrieved April 2012, from NASA: http://www.nasa.gov/centers/langley/news/factsheets/X43A_2006_5.html
5. E. T. Curran and F. E. Stull, Aero Propulsion Lab., RTD-TDR-63-4097, (1964)
6. E. T. Curran, W. H. Heiser, and D. T. Pratt, *Annual Review of Fluid Mechanics*, **28**, 323-360, (1996)
7. W. H. Heiser, and D. T. Pratt, *Hypersonic Air Breathing Propulsion*, AIAA Education Series, AIAA, Washington, D.C., (1993)
8. S. Emami, C. A. Trexler, A. H. Auslender, and J. P. Weidner, *NASA TP-3502*, May (1995)
9. C.-P. Wang, K.-Y. Zhang, and K.-M. Cheng, *AIAA Paper 2006-818*, (2006)
10. N. Bachchan, and R. Hillier, *AIAA Paper 2004-4716*, (2004)
11. K. Matsuo, Y. Miyazato, and H.-D. Kim, *Progress in Aerospace Sciences*, **35**, 1, 33-100, (1999)
12. P. J. Waltrup, and F. S. Billig, *AIAA Journal*, **11**, 10, 1404-1408, (1973).
13. P. J. Waltrup, and F. S. Billig, *Journal of Spacecraft and Rockets*, **10**, 9, 620-622, (1973)
14. B. U. Reinartz, C. D. Herrmann, and J. B. Ballmann, *Journal of Propulsion and Power*, **19**, 5, 868-875, (2003)
15. G. Sullins, and G. McLafferty, *AIAA Paper 92-5104*, (1992)
16. C.-J. Tam, K.-C. Lin, D. L. Davis, and R. Behdadnia, *AIAA Paper 2006-4509*, (2006)
17. S. K. Stouffer and M. A. Hagenmaier, *AIAA Paper 2001-0519*, (2001)
18. J. A. Hudgens, and C. A. Trexler, *AIAA Paper 92-3101*, (1991)
19. G. Masuya, T. Komuro, A. Murakami, N. Shinozaki, A. Nakamura, and O. Murayama, *Journal of Propulsion and Power*, **11**, 2, 301-307, (1995).
20. D. M. Van Wie, F. T. Kwok, and R. F. Walsh, *AIAA Paper 96-2914*, (1996)
21. J. L. Wagner, K. B. Yuceil, A. Valdivia, N. T. Clemens, and D. S. Dolling, *AIAA Journal*, **47**, 6, 1528-1542, (2009)
22. J. L. Wagner, K. B. Yuceil and N. T. Clemens, *AIAA Journal*, **48**, 9, 1875-1888, (2010)